3D Printing of Aqueous Two-Phase Systems with Linear and Bottlebrush Polyelectrolytes

Zichen Jin[b], Hong-Gyu Seong[b], Satyam Srivastava[b], Alex McGlasson[b], Todd Emrick[b], Murugappan Muthukumar[b], Thomas P. Russell*[a,b]

[a] Prof. T. P. Russell
Materials Sciences Division
Lawrence Berkeley National Laboratory
1 Cyclotron Road, Berkeley, CA, 94720, USA
E-mail: russell@mail.pse.umass.edu

[b] Z. Jin, H.-G. Seong, Dr. S. Srivastava, A. McGlasson, Prof. T. Emrick, Prof. M. Muthukumar, Prof. T. P. Russell
Department of Polymer Science and Engineering Department
University of Massachusetts
120 Governors Drive, Amherst, MA 01003 USA

Abstract: We formed core-shell-like polyelectrolyte complexes (PECs) from an anionic bottlebrush polymer with poly (acrylic acid) side chains with a cationic linear poly (allylamine hydrochloride). By varying the pH, the number of side chains of the polyanionic BB polymers (N_{bb}), the charge density of the polyelectrolytes, and the salt concentration, the phase separation behavior and salt resistance of the complexes could be tuned by the conformation of the BBs. By combining the linear/bottlebrush polyelectrolyte complexation with all-liquid 3D printing, flow-through tubular constructs were produced that showed selective transport across the PEC membrane comprising the walls of the tubules. These tubular constructs afford a new platform for flow-through delivery systems.

Introduction

Vascular networks extensively pervade most tissues in the body, playing critical roles for oxygen and nutrient delivery, as well as waste product removal.[1] For several decades synthetic polymer systems, including polyelectrolyte complexes (PECs), have been developed to mimic these membranous constructs for drug delivery, encapsulation and sensing.[2] Numerous processing strategies have been used, including microfabrication and extrusion bioprinting, to achieve this end with aqueous two-phase systems (ATPSs).[3] The interfacial tension between the two different aqueous solutions is exceptionally small, markedly enhancing the stability of the phase separated structures. The most commonly used ATPSs are aqueous solutions of polyethylene glycol (PEG) against aqueous solutions of dextran (DEX) or aqueous solutions of mixtures of a polymer, like PEG, and a salt, such as potassium phosphate (K_3PO_4), where the immiscibility is dictated by the concentration of the components. [4]

Numerous studies have investigated PECs formed with linear polyelectrolytes (L-PEs).[5] Using combinations of experimental, theoretical, and simulation approaches, electrostatic forces (charges), hydrogen bonding, dipolar interactions, van der Waals interactions (including excluded volume effects), and chain connectivity have emerged as the key variables in these systems.[2],[5],[6] Electrostatic interactions and entropy have been identified as the major driving forces underpinning the phase separation of PECs.[6],[7] Factors influencing the electrostatic interaction energy between charged polymers include composition, temperature (related to segmental interactions, the χ parameter) and the Bjerrum length (l_B).[6],[8] PEs can be classified as either weak or strong depending on their degree of ionization in solution. Strong PEs can be dissolved over a wide range of pH without significant charge differences. Weak PEs have weak ionic functional groups and are strongly influenced by changes in pH.[9] A recent computational study by Whitmer, *et al*. reported that entropic contributions dominate the free energy of strong PECs. However, in weak PECs the influence of entropy can be weakened by associative charging, chain branching, and molecular weight.[10]

Bottlebrush polymers (BBPs) feature polymer chains densely grafted onto a linear backbone, where the conformation of the BBP depends on the number of repeat units in the backbone (N_{bb}) relative to the number of repeat units in the side chains (N_{sc}). Verduzco and coworkers, using small-angle neutron scattering (SANS) and small-angle X-ray scattering (SAXS), showed that the conformation of BBPs in solution vary from spherical to cylinder-like to worm-like depending on the ratio of N_{bb}/N_{sc}.[5],[11] Theoretical simulations and arguments by Dutta and Rathgeber support such conformational changes in BBPs.[12] These conformational variations make BBPs excellent candidates as lubricants, templates and scaffolds for inorganic materials across multiple length-scales. Super-resolution images and simulation studies of BBP melts also show evidence for these conformational transitions as a function of N_{bb}/N_{sc}.[11] Lawrence and coworkers investigated the impact of side

chain dispersity and backbone chain molecular weight using pressure-area isotherms of Langmuir monolayers.[11] Scanning electron microscopy (SEM), transmission electron microscopy (TEM), and SAXS have been widely used to investigate the self-assembly and micelle formation of amphiphilic symmetric or asymmetric bottlebrush random copolymers or bottlebrush block copolymers (BBCPs).[11],[13]

Previous studies have extensively investigated cationic bottlebrush polyelectrolytes (BB-PEs), and bottlebrush / bottlebrush polyelectrolyte complexes (BB/BB-PECs) formed between the cationic BB-PEs

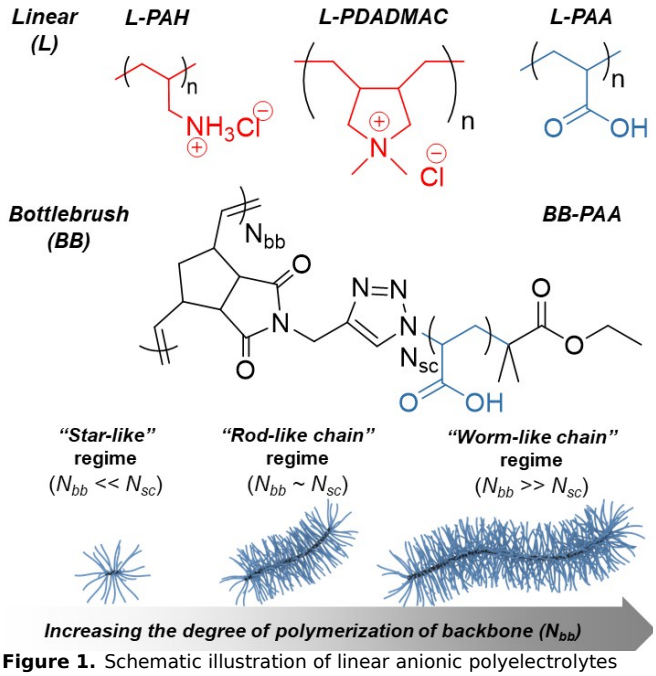

Figure 1. Schematic illustration of linear anionic polyelectrolytes (anionic L-PEs) labelled blue, linear cationic polyelectrolytes (cationic L-PEs) labelled red and bottlebrush polyacrylic acid (BB-PAA) with side chains(blue) and backbone chain(black).

and anionic BB-PEs.[5],[6],[13],[14] Here, we investigated functional BB-PECs using an anionic bottlebrush poly (acrylic acid), BB-PAA, with cationic L-PEs, specifically poly (allylamine hydrochloride), L-PAH, and diallyldimethylammonium chloride, L-PDADMAC. By varying N_{bb}, the influence of the BB-PE conformation (**Figure 1**) on the characteristics of the PECs was investigated. A particular advantage of the anionic BB-PEs, in comparison to cationic BB-PEs, is the ease of synthesis of polymers with lower polydispersity (PDI) and higher N_{bb}.[14] The phase behavior, morphologies and solution dynamics of the BB-PECs were compared to the corresponding all-linear PECs (L-PECs) systems. Our findings show a broadening of the phase diagrams and an increased resistance to the addition of salt for BB-PEC systems, that increases with increasing N_{bb}. The BB-PECs from cationic L-PAHs with anionic BB-PAAs were found to have sizes larger than those from L-PECs that increased as N_{bb} increased. Due to the crowding of the ionic units on the side chains of the anionic BB-PEs, particularly near the backbone chain, morphological transitions from spherical-like to core-shell-like are observed.

We used BB-PECs for all-aqueous 3D printing, to overcome challenges arising from the weak interactions and unstable structure formation in L-PEC systems and enable the printing of tubules shrouded in a BB-PEC membrane. Due to the asymmetry in charge across the interface,[4] there is selective transport through the membranes that serve as unique small and large molecule delivery vehicles, expanding the potential application of weak polyelectrolyte complexes. Due to the heightened sensitivity of weak polyelectrolytes to variations in salt concentration and pH levels, as compared to the typically more stable strong polyelectrolyte complexes, this newly formed polyelectrolyte complex transport membrane can be used under different salt and pH conditions.

Results and Discussion

BB-PAA, shown in **Figure 1**, was used with N_{sc} = 37 repeat units and the backbone chain length, N_{bb}, varied from 20 to 500. All BB-PAAs were synthesized by ring-opening metathesis polymerization[15] (characterization details provided in the Supporting Information). Commercially available linear polyacrylic acid (L-PAA) having 550 repeat units of carboxylic function groups was used as the anionic L-PE. Commercially available linear poly (allylamine hydrochloride) (L-PAH) with 700 repeat units, each having an amine functional group and linear poly (diallyldimethylammonium chloride) (L-PDADMAC, molecular weight MW 200-350 kDa), were used as the cationic L-PEs (**Figure 1**).

Table 1. Molecular Weights, Radii of Gyration, Hydrodynamic Radii and Shape Factors of PAA

Sample	PAA (N_{bb})	$M_{n,SEC}$ (kDa) [15]	PDI[15]	R_g (nm) [a]	R_H (nm) [a]	s
L-PAA	----	50	1.53	7.15	4.9 ± 0.2	1.46
BB1-PAA	20	91	1.25	3.1 ± 1.4	2.7 ± 1.1	1.17
BB2-PAA	50	236	1.15	3.4 ± 1.4	2.9 ± 0.3	1.18
BB3-PAA	100	490	1.18	5.3 ± 1.9	4.3 ± 0.2	1.25
BB4-PAA	200	899	1.19	9.7 ± 5.3	6.4 ± 0.1	1.5
BB5-PAA	500	2393	1.21	13.3 ±	7.1 ±	1.87

		5.1	1.4

[a] polymer solutions in 0.5M NaCl at pH 6.5

Figure 2. Shape factors, **s** (=R_g R_H^{-1}), of the BB-PAAs as a function of N_{bb} (right Y-axis) using light scattering under 0.5M NaCl, pH 6.5 and pKa of the BB-PAAs as a function of N_{bb} (left Y-axis) under 0.25M NaCl.

Solution Characteristics of PEs

Static and dynamic light scattering was used to measure the radii of gyration (R_g), hydrodynamic radii (R_H), and the shape factors (R_g R_H^{-1}) of the BB-PAAs (summarized in **Table 1**). The increases in R_g were correlated with increases in N_{bb}, and the different relationships between R_g and N_{bb} are attributed to the shape transitions of the BB-PAAs (**Figure 2**). When $N_{bb} < N_{sc}$, i.e., the lengths of side chains are longer than the length of the backbone and the polymer assumes a star-like conformation. When $N_{bb} \sim N_{sc}$, the backbone begins to influence the conformation of the chain, but the side chains still play a significant role leading to an increase in R_g and a transition in the shape from star-like to ellipsoidal. When $N_{bb} >> N_{sc}$, the backbone dominates the conformation, causing the chain to assume a worm-like chain conformation. R_g follows a power-law relationship with N_{bb} ($R_g \sim N_{bb}^{\nu}$) with $\nu = 0.7$ under salt-free conditions.[16] $\nu = 0.59$ under 0.5M NaCl conditions (**Figure S2**) indicating that the polymers are in a good solvent. R_H is also affected by N_{bb} and pH, since PAA is a weak polyelectrolyte. Monte Carlo simulations show that R_H follows a power-law relationship with N_{bb} ($R_H \sim N_{bb}^{\nu}$) with $\nu = 0.6$ under salt-free conditions.[16] $\nu = 0.3$ under 0.5M NaCl conditions (**Figure S4**) at neutral pH, indicating that the polymers are globular-like. The BB-PAA shape factor, ***s*** = R_g R_H^{-1}, determined by light scattering, as shown in **Figure 2**, increases as N_{bb} increases, indicating a transition from a star-like (for N_{bb} = 20) to a worm-like (for N_{bb} = 200 and 500) confirmation. The anionic BB-PAAs with intermediate chain lengths (N_{bb} = 50 and 100) show a rod-like chain conformation, in the transition regime between star-like and worm-like conformations.[12] Since acrylic acid is pH sensitive, R_H changes from 5.98 nm (pH 4.5) to 7.12 nm (pH 8.5) (**Figure S5**).

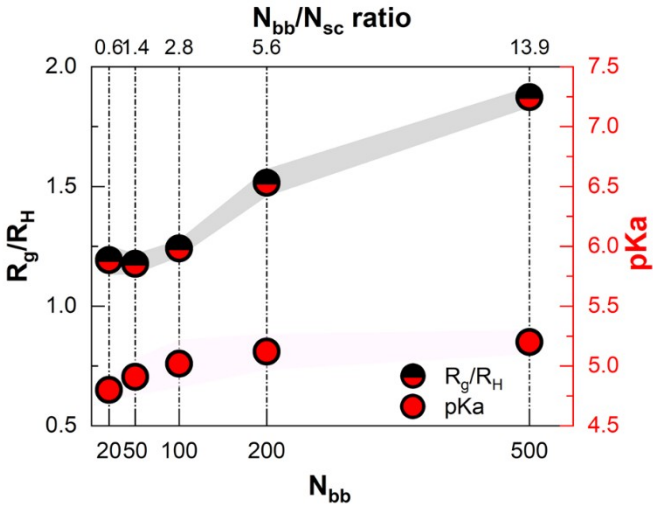

These findings are consistent with intrinsic viscosity ([η]) measurements (**Figures S6, S7**). From the Flory-Fox equation,[16b]

$$[\eta] = \frac{\phi \left(r^2\right)^{3/2}}{\acute{M}} \qquad (3)$$

Where $[\eta]$ is the intrinsic viscosity, $\acute{M}$ the average molecular weight, ϕ the Flory constant, and r the end-to-end distance. For L-PAA, $[\eta]$ $M^{0.72}$, consistent with the literature, indicating that the polymers are in a good solvent (**Figure S6**).[12] For BB-PAAs, there are two scaling exponents for [η], depending on ***s*** or N_{bb} (**Figure S7**), since N_{SC} is fixed. At low N_{bb}, the exponent is 0.26, indicating that the polymer is more star-like, with the backbone chain length having little impact on [η].[12],[16] At high N_{bb}, the exponent is 0.69, comparing well to the literature value of 0.73,[12],[16],[17] reflecting the increased importance of the backbone chain length on the worm-like conformation (**Figures S6** and **S7**).

Degree of Ionization

For BB-PEs, the extent to which the ionic groups on the side chain can be deprotonated depends on the lineal density of side chains attached to the backbone chain, the distance between the ionic groups and the mains chain, and the conformation of the chain. Since PAA is pH responsive,[5],[18] the pKa and degree of ionization of BB-PAA and L-PAA were determined by titration. We found that the pKa depended on the conformation of the BB-PEs, indicating that repulsive interactions due to backbone chain crowding was important. The pKa of BB-PAA is more basic than L-PAA, in keeping with this, and for all BB-PAAs, the pKa values increase with N_{bb} (**Figure 2**), but not linearly. The anchoring of side chains to every backbone unit gives rise to a dense packing of ions that increases with increasing backbone length, making BB-PAAs relatively less acidic and less nucleophilic, since neighboring charges disfavor deprotonation due to electrostatic repulsion. Previous study of Bapolisi et al.[19] on weak cationic polymer brushes grafted to a solid substrate showed similar behavior, where the increased aerial density of grafted chains led to a suppression of the ionization of charged amine units near the backbone chain, effectively decreasing the pKa relative to the chain length. The acid/base balance for polyelectrolyte chains, relating pH to the degree of deprotonation/ionization for dilute PAA,[20] is given by:

$$pH = pK_{a(app)} + n_H \log \frac{\alpha}{1-\alpha} \qquad (4)$$

where α is the degree of ionization and $pK_{a(app)}$ is apparent acid/base dissociation constant of the polyelectrolyte. Based on the degree of ionization curve

(**Figure S8**), BB-PAA intersects that of the cationic L-PE at a maximum degree of ionization at ~pH of 6.5. At pH 9, PAA is fully charged, reaching a plateau, corresponding to the fully neutralized condition. For all PECs at pH = 6.5, the condition used in our studies, ~ 90% of the PAA is ionized, representing a partially neutralized condition.

Polyelectrolyte Complex (PEC) Formation and Characteristics

The formation of BB-/L-PECs using BB-/L-PAA and L-PAH is seen in the optical micrographs (OM) in **Figure S10**. At low or no salt conditions, a white precipitate is observed (**Figures S9a and S9b**). The addition of salt induces the formation of a coacervate phase (**Figure S9c1, c2**), and at high salt concentrations, the system clears, due to charge screening, when free ions balance the electrostatic charges. As a result, the turbidity decreases with more salt addition and the refractive index difference between the complex and supernatant decreases (**Figure S9d**). Turbidity measurements (**Figure 3A**) align with the OM results. All PECs showed an increase in the turbidity for low salt concentrations (0.05 – 0.2 M NaCl), while at higher salt concentrations (0.3 – 1M NaCl) coacervation occurs, and with a further increase in salt concentration, the PEC is solubilized. The BB-PECs show higher intensities in both the precipitate and coacervate regimes, in comparison to the L-PECs. At 2M NaCl, the intensity of L-PEC plateaus at a low value (0.05-0.10), indicating a salt resistance of 2M NaCl, while BB-PECs show a higher salt resistance, maintaining a turbidity of 0.2 at 2M, slightly increasing at 3M NaCl, with the generation of secondary aggregates, due to the stronger electrostatic interactions between sodium ions and the PECs formed with BB-PAAs (**Figure 3A**). L-PECs exhibit a similar

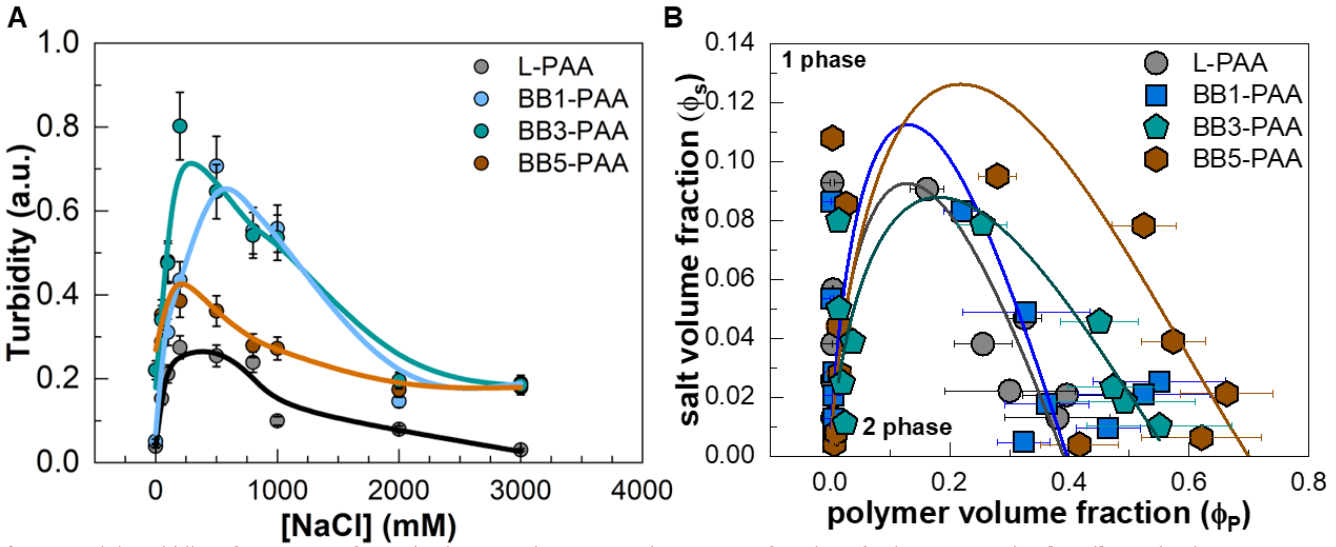

Figure 3. (A) Turbidity of L-/BB-PECs formed using L- and BB-PAA and L-PAH as a function of salt concentration [NaCl]. Total polymer concentration C_p=0.05% wt; polycation/polyanion ratio of 1; pH for L-PAA, BB-PAA and L-PAH are all pH 6.5. (B) Phase diagram of L-PEC (gray dot), BB1-PEC (blue dot), BB3-PEC (green dot) and BB5-PEC (brown dot). Total polymer concentration Cp=0.5% wt; polycation/polyanion ratio of 1; pH for L-PAA, BB-PAA and L-PAH are all pH 6.5.

behavior at a higher concentration of NaCl, as reported by Li and coworkers.[21]

The phase diagrams providing the compositions of the complex and supernatant phases were determined by thermogravimetric analysis (TGA) (detailed in SI). **Figure 3B** shows the phase boundaries for L-PECs, BB1-PECs, BB3-PECs and BB5-PECs with total polymer concentrations of C_p = 0.05% wt (including both the BB- and L-PEs) at neutral conditions (pH=6.5) shown as the volume fraction of salt Φ_S as a function of the volume fraction of polymer Φ_P (**Figure 3B**). The phase boundaries for BB-PECs are broader than for L-PECs. The larger backbone units of BB-PAAs, e.g., like BB3-PEC and BB5-PEC, showed even larger composition differences than BB1-PEC at the same salt composition and a higher salt resistance (**Figure 3B**). Optical microscopy measurements of the complex size (**Figure S11**) show a similar trend as a function of salt concentration. For highly charged polymers, like BB-PAAs, computational studies showed entropy to be important for PEC formation, except for weak polyelectrolyte systems.[11],[22] The shape factor of BBPs strongly correlates with the entropy of the system. As N_{bb}/N_{sc} increases, the conformational entropy difference first decreases and then increases, with a minimum at N_{bb}/N_{sc}~1.[23] Star-like (BB1-) PAA, with N_{bb}/N_{sc}~0.54, leads to higher aggregation numbers, promoting BB1-PEC formation. Rod-like (BB1-) PAA, with a ratio of N_{bb}/N_{sc}~2.7, and worm-like (BB5-) PAA, with a ratio of N_{bb}/N_{sc}~13.5, lead to more aggregations, thereby broadening the PEC phase envelope, due to the increase in conformational entropy with increasing in N_{bb}/N_{sc}. (**Figure 3B**). This behavior can also be interpreted in terms of steric hinderance from the high linear density of charged side chains. Deprotonation of the densely-grafted side chains near the backbone chain, which contain a higher density of negative charges, is more challenging.[5],[23],[24]

The size and shape of PECs observed by OM (**Figures S10**), AFM (**Figure S11**), and SEM (**Figure S12**) depend on the

conformation of PAA. The volume pervaded by the L-PAAs is, to a first approximation, spherical in shape, while that for BB-PAAs varies depending on ***s*** (**Figure S10**). PECs from star-like BB-PEs form droplets, since they can easily associate with several flexible, charged L-PEs, due to the more open side chain ionic interaction volume. This results in a greater number of ionic interactions at a lower pKa. For worm-like BB-PEs, L-PAHs can interact more easily with the side chains at both ends of the BB-PEs (BB-PAA) to form a core-shell structure, where the outer portion is thicker and charge neutral, while the inner portion remains thinner and negatively charged (**Figures S10**). This is attributed to the greater flexibility of the side chains at the ends and outer edges of the BB-PAA, enabling easier penetration of the L-PAH into the brush in comparison to the more densely packed side chains near the backbone chain.

The conformation of BB-PAAs, as determined by static and dynamic light scattering in **Figure 4A** and **S13**, has a significant impact on the hydrodynamic radius of the PECs in the supernatant, The intensity varies as $I \propto q^{-v}$ (where v ranges from 0 to 4),[25] reflecting the conformation of the supernatant complexes. Complexes are formed with α =1.1, corresponding to a rod-like structure. Conversely, for complexes formed between L-PAH and star-like BB-PAAs (BB1-PAA), α =2.3 corresponding to a dense mass fractal object (**Figure 4**). For complexes formed between L-PAH and more rod-like BB-PAAs (BB3-PAA), α =1.74, indicating a more open mass fractal-like conformation (**Figure 4**). For complexes formed between L-PAH and worm-like BB-PAAs (BB5-PAA), α =1.9 corresponding to sparse mass fractal- or disc/lamella-like conformation (**Figure 4**). Conversely, the observed core-shell structure of the PEC is reasonable. The denser mass fractal of star-like-BB1-PEC compared to the rod-like-BB3-PEC indicates that rod-like-BB3-PAA has a lower probability of interacting with L-PAH due to the rigidity of its conformation. These findings were further supported by AFM (**Figure S11**) and SEM (**Figure S12**) measurements of the L-/BB-

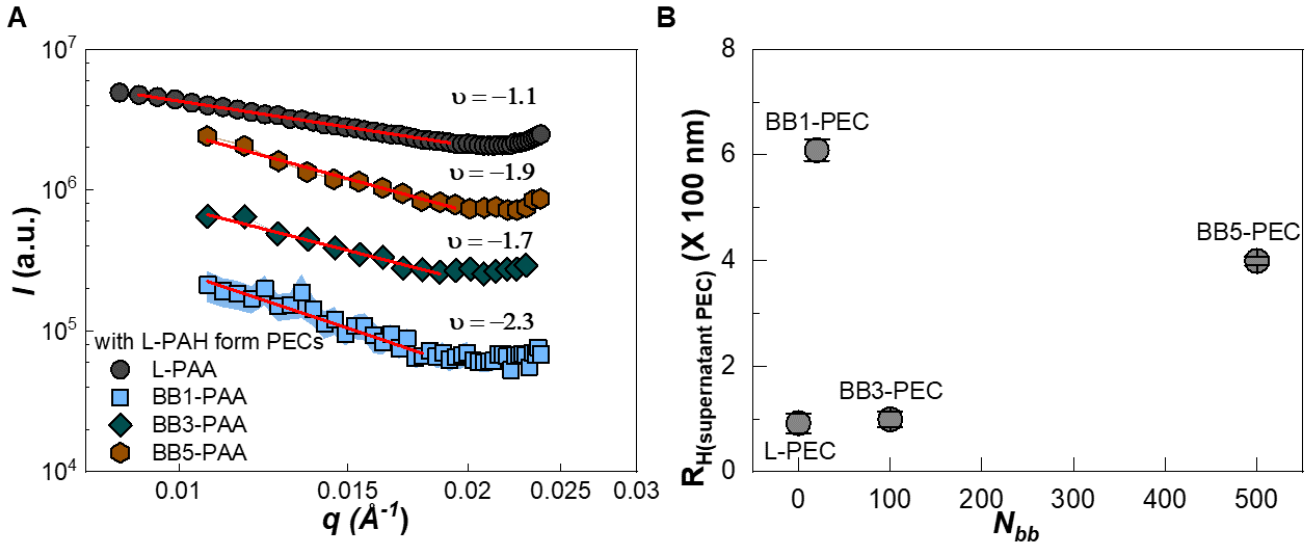

Figure 4. (A) log- scattering intensity versus scattering vector q plots obtained from static light scattering of the supernatant phase of L-/BB-PECs under 1:1 polycation/polyanion ratio and 0.5M NaCl under C_p=0.05 wt%. The numerical values along the y-axis do not accurately depict precision; for enhanced clarity, the data plot has denormalization by exhibiting each pair of intensities a tenfold difference to mitigate potential overlap. (B) Size of L-/BB-PECs formed from complexation by dynamic light scattering of the supernatant phase.

PECs drop-cast onto Si wafers. The AFM height profile of L-PECs from L-PAH and L-PAA (**Figure S11**) shows no obvious features on the dried films. AFM scans of dried films of BB5-PECs from L-PAH and BB5-PAA (N_{bb} = 500) show structures having two distinct peaks, characteristic of a core-shell structure (**Figure S11**). AFM scans of dried films of BB1-PECs from L-PAH and BB1- PAA (N_{bb} = 20), on the other hand, show a Gaussian-like height profile (**Figure S11**), as would be expected from the star-like conformation of the BB1-PAA. We note that SEM images (**Figure S11**) show evidence for a core-shell structure. In the SEM micrographs, the edges of the BB5-PECs are slightly brighter suggestive of a core-shell structure (**Figure S12**).

The size of the complexes in the supernatant phase were measured by DLS. In **Figure 4B**, the R_H of the different L-/BB-PECs in the supernatant phases are shown for C_p = 0.05wt%, with a 1:1 polycation/ polyanion ratio, and a salt concentration of 0.5 M NaCl. The star-like (BB1-) PEC is largest, followed by worm-like (BB5-) PECs, then the cylinder-like (BB3-) PECs, with the L-PECs being the smallest, due to the conformations of the BB-PAAs, where the rigidity of the backbone chain inhibits effective interactions. The sparse mass fractal configuration of the BB3-PECs from the cylinder-like-(BB3-) PAAs suggests that the rigid side and backbone

chains inhibit polycation chain penetration. The BB-PECs with the star-like-(BB1-) PAAs have more open architectures with negatively charged ions, enabling increased interactions with the cationic ions from L-PAH.

All-Aqueous 3D Printing

For all-liquid printing, reducing the interfacial tension is important to avoid the Plateau-Rayleigh instability[26] that causes a breakup of the jetted liquid in droplets. With ATPSs the IFT is quite low at ~ 0.1 mN m^{-1}, and the oppositely charged PEs in the two aqueous phases diffuse to and interact with each other at the ATPS interface, forming a PEC complex. The density of 4 wt% PEG solution (1.004 g mL^{-1}) is only slightly lower than that of 10wt%

dextran (1.015 g mL^{-1}), significantly reducing deformation of the structures due to gravitational forces. Other factors that influence droplet formation include the diameter of the fluid stream being jetted, the jetting speed, and the viscosities of both the jetted fluid and the medium solution. Stabilization of the printed structures depends on a competition between the kinetics of the assembly, including the diffusion of the L-/BB1-PAA and L-PAH to the interface, kinetics of the interactions at the interface, and the stabilization of the interface by the assembly of the complexes, and the coarsening of the constructs printed that is driven by the minimization of the interfacial area or interfacial tension, and the viscosities of the fluids. All were investigated to determine conditions under which stable jets could be printed and stabilized by the formation of L-/BB1-PECs at the interface between the two aqueous phases. These are described in the Supporting Information.

The printing behavior of several different PEC systems is shown in **Figures S14**. L-PDADMAC with L-PAA (**Figure S14-B3**) does

not immediately form a continuous thread or tubule after printing. L-PAH with L-PAA initially forms a thin transparent 0.6 mm diameter tubular spiral that vanishes after 30 minutes (**Figure S14-B1**). By replacing L-PAA with BB1-PAA, a stable BB1-PEC is formed (**Figure S14-B2/4**). BB1-PAA interacts with L-PAH and L-PDADMAC to produce continuous semi-transparent threads that swell (22% and 7%, respectively), become opaque after half hour, and then remain stable for at least 24 hours (**Figure S14-B2/4**). Optical microscopy shows the formation of the L-/BB1-PECs (**Figure 5** and **S14**). For L-PAA with L-PAH/PDADMAC, the L-PECs partially form on the surface of the membrane. However, for BB1-PAA with L-PDADMAC, a strong BB1-PEC system, a double layered membrane is observed, where the outer membrane, on the PEG-rich side of the ATPS, forms initially as the PAH diffuses into the BB1-PAA rich dextran phase. As the diffusion of the PAH into the BB1-PAA-rich dextran phase proceeds, clear evidence of a phase separated morphology is seen, similar to the blastasome-like morphology reported by Zhu et al.,[27] where BB1-PEC forms on the walls of the phase-separated domain. With diffusion of the L-PAH and BB1-PAA slowed through this phase separated morphology, a second membrane forms further encapsulating the dextran-rich phase being jetted from the needle. (**Figure 5B**). Since the tubules are flow through, they afford a convenient platform to probe the transport characteristics of the PEC membranes without the need of spin coating or layer-by-layer methods, as done in previously.[28]

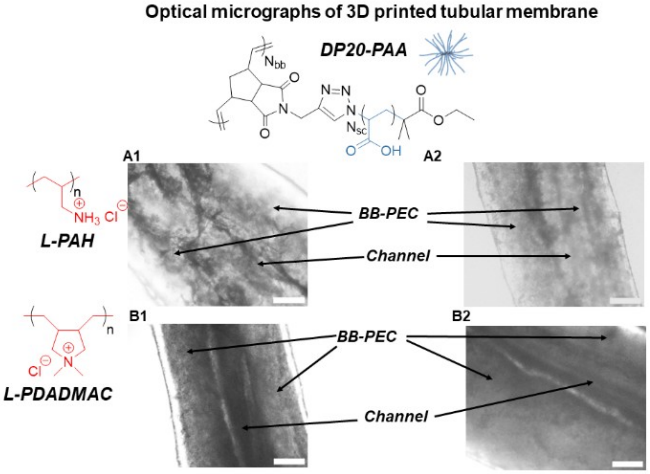

Figure 5. All-aqueous 3D printed tubules where PECs of PAA and BB-PAAs form a membrane encasing flow-through tubules, A1 and A2 BB1-PEC formed with L-PAH with BB1-PAA; B1 and B2 BB1-PEC formed with L-PDADMAC and BB1-PAA.Scale bars in images are 500 μm.

Diffusive Membranes

Ion exchange leads to osmotic pressure within the tubule. The pressure differential between the supply source within the membrane and the reservoir outside of the membrane results in the diffusion of ions or molecules across the membrane. Here we investigated the diffusion across membranes formed by L-/BB1-PAA in the dextran phase and L-PAH and Rhodamine B(RB) in the PEG phase (Cases II and IV), and L-/BB1-PAA with RB in the PEG phase and L-PAH in the dextran phase (Cases I and III) as shown schematically in **Figure 6**. The increase in the concentration of RB was used to assess the diffusion across the membrane formed at the interface between the two liquid layers.

A 1:10 ratio of the PEG and dextran phase was used to measure the transport properties (**Figure S16**). The concentration of RB in the PEG phase is measured over a 12 h period (**Figure 6** and **S16**). As shown in **Figure 6**, the concentration of RB increased linearly with time during the initial several hours and reached a plateau at 20.1 μM after ~ 6h for Case I, 10.4 μM after ~7 h for Case II, 8.5 μM after ~10h for Case III and 5.12 μM after ~12 h for Case IV (**Figure 6, Table S5**). Ignoring the effects of concentration related to charge, assuming the ion transport through membrane is constant, Fick's second law of diffusion,[29]

$$\frac{dc}{dt} = D\frac{d^2c}{dx^2}$$

where $\frac{dc}{dt}$ is the change of concentration with time over a distance *x* in a time *t*, and D is the diffusion coefficient.

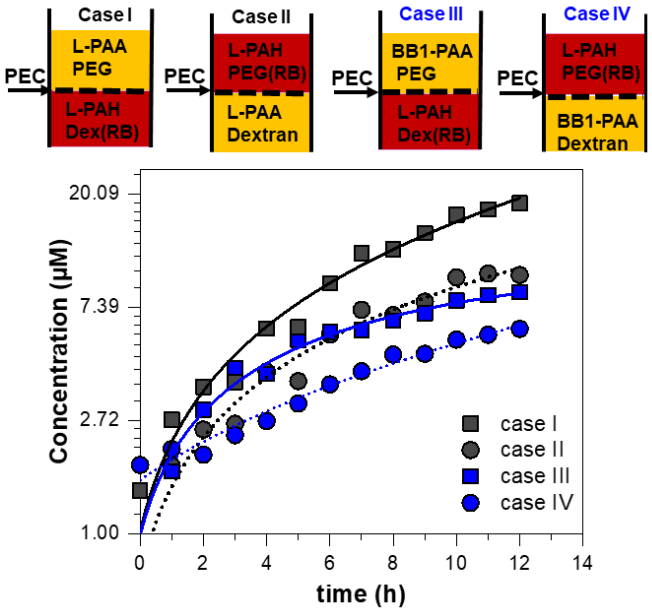

Figure 6. Ion transport behaviour for L-/BB1-PEC in an ATPS. Schematic of four cases under two aqueous systems. Rhodamine B concentration change with time in PEG phase (case I and III) and dextran phase (case II and IV) as displayed.

The diffusion coefficients of RB in the PEC-formed membranes in the four different cases varied from ~1.1 X 10^{-12} m^2 s^{-1} (Case IV) to 1.3 X 10^{-11} m^2 s^{-1} (Case I). Literature indicates that RB in a bulk solution has a diffusion coefficient of (2.69 ± 0.02) X10^{-10} m^2 s^{-1} in a methanol/aqueous buffer based on static imaging,[30] and RB in PEGDA-575/HEA membranes has a coefficient of 5 X 10^{-11} m^2 s^{-1}.[31] The measurements for Case I (1.3 X 10^{-11} m^2 s^{-1}) is in good agreement with literature, (**Figure 6, Table S5**). However, for Cases II (1.6 X 10^{-12} m^2 s^{-1}), III (3.0 X 10^{-12} m^2 s^{-1}) and IV (1.1 X 10^{-12} m^2 s^{-1}) the diffusion coefficient is one order magnitude smaller than the literature membrane diffusion coefficients and about two orders magnitude order smaller than in the bulk solution (**Figure 6** and **S18, S19, S20 and Table S5**).[26],[31],[32] The data suggests that the L-PEC membrane behaves as a highly permeable structure, as the diffusion coefficient of RB is only slightly slower than the diffusion of L-PEC in bulk solution. On the other hand, the BB1-PEC membranes are less permeable, due to the more crowded complexes and structures formed within the membrane.[33] The viscosity of the ATPS medium and jetted solution would lower the diffusion coefficient, which explains why the measured data in **Figure 6** are lower than literature values in methanol/aqueous buffer.[30],[34] Additionally, when compared to the diffusion coefficient of ~5.5X 10^{-16} m^2 s^{-1} through 2 bilayers of L-PSS/L-PAH[33] and the diffusion rate of Methylene Blue(MB) through 10.5 bilayers of L-PAA/L-PAH[35] (~10^{-18} m^2 s^{-1}), the diffusion coefficient through single PEC membrane formed by 3D printing(**Table S5**) is much faster. Furthermore, the RB diffusion coefficient for PEG into dextran (Case II/IV) and dextran into PEG (Case I/III) also differ. In general, the diffusion coefficient of RB from dextran into PEG is higher, since the membrane is thinner, PAH slightly favors partitioning in PEG, and PAA favors dextran, as reported by Chao et al.[32] The less permeable membrane generated by BB1-PEC is of interest to reduce the diffusion coefficient of particles penetrating the membrane, especially large particles, e.g., anticancer drug molecules like Doxorubicin (DOX) (detailed in SI, **Figure S21-24**).[36]

Conclusion

This work introduces a novel class of BB-PEC systems made from BB-PAA and L-PAH. The conformation of the BB-PAA chains undergo transitions from star-like, rod-like, and worm-like chains as N_{bb}/ N_{SC} increases. BB-PAA was found to have a higher *pKa* than L-PAA, due to the densely grafted charged BB-PAA chains, making deprotonation more challenging.

The phase behavior and properties of BB-PECs are dependent on the polymer conformation of BB-PAAs, generally showing a broader phase diagram and increased salt resistance. The size and morphology of BB-PECs are also influenced by the conformation of BB-PAAs. Worm-like PAA forms networks with L-PAHs that reconfigure to form larger elliptical and core-shell morphologies. This core-shell morphology arises from the increased flexibility of the backbones in worm-like conformation and difficulty in deprotonating segments close to the backbone.

We demonstrated that this new BB-PEC system can be combined with an ATPS to generate stable tubular structures using all-liquid 3D printing. This newly developed BB-PEC generates a denser and less permeable membrane, thereby reducing the ion transport rate. This innovation broadens the platform for the ion transport delivery system using weak polyelectrolytes.

Supporting Information

The authors have cited additional references within the Supporting Information.[34],[35],[36],[37],[38],[39],[40],[41],[42]

Acknowledgements

This work was supported by the Army Research Office under W911NF-24-2-0041, AFOSR (Grant No. FA9550-21-1-0388), and National Science Foundation (Grant No. DMR 2309539).

Keywords: Bottlebrush Polyelectrolytes• Polyelectrolyte Complexation• 3D Liquid Printing• Transport

[1] a) C. O'Connor, E. Brady, Y. Zheng, E. Moore, K. R. Stevens, *Nat Rev Mater* **2022**, *7*, 702-716; b) D. A. Beard, J. B. Bassingthwaighte, *Ann Biomed Eng.* **2001**, *4*, 298-310; c) R.

Monahan-Earley, A. M. Dvorak, W. C. Aird, *J. Thromb. Haemost*. **2013**,*11*, 46–66; d) A. M. Jorgensen, J. J. Yoo, A. Atala, *Chem. Rev*. **2020**, *12*0, 11093–11127.

[2] a) S. L. Perry, L. Leon, K. Q. Hoffmann, M. J. Kade, D. Priftis, K. A. Black, D. Wong, R. A. Klein, C. F. Pierce, K. O. Margossian, *Nat. Commun*. **2015**, *6*, 6052; b) L. Zhao, M. Skwarczynski, I. Toth, *ACS Biomater. Sci. Eng.* **2019**, *5*, 10, 4937-4950; c) T. D. Harrison, O. Yunyaeva, A. Borecki, C. C. Hopkins, J. R. Bruyn, P. J. Ragogna,E. R. Gillies, *Biomacromolecules* **2020**, *21*, 1, 152-162; d) M. A. J. Mazumder, F. Shen, N. A. Burke, M. A. Potter, H. D. H. Stöver, *Biomacromolecules* **2008**, *9*, 9, 2292-2300.

[3] a) W. Zhang, Q. Zhao, J. Yuan, *Angew. Chem. Int. Ed.* **2018**, *57*, 6754-6773; b) R. Costa-Almeida, L. Gasperini, J. Borges, P. S. Babo, M. T. Rodrigues, J. F. Mano, R. L. Reis, M. E. Gomes, *ACS Biomater. Sci. Eng.* **2017**, *3*, 7, 1322-1331; c) R. R. Costa, D. Caballero, D. S. da Costa, R. Rodriguez-Trujillo, S. C. Kundu, R. L. Reis, I. Pashkuleva, *Advanced Materials Technologies* **2023**, *8*, 2300983; d) L. Zhang, L.-H. Cai, P. S. Lienemann, T. Rossow, I. Polenz, Q. Vallmajo-Martin, M. Ehrbar, H. Na, D.J. Mooney, D. A. Weitz, *Angew. Chem.* **2016**, *128*, 1-6.

[4] a) C. Liu, Y. W. Tong, *ACS Appl. Mater. Interfaces* **2023**, *15*, 17, 20712-20725. b) M. T. Zafarani-Moattar, S. Hamzehzadeh, S. Nasiri, *Biotechnol. Progr.* **2011**, *28*, 146-156; c) G. Xie, J. Forth, Y. Chai, P. D. Ashby, B. A. Helms, T. P. Russell, *Chem* **2019**, *5*, 10, 2678-2690; d) M. Mastiani, N. Firoozi, N. Petrozzi, S. Seo, M. Kim, *Scientific Reports* **2019**, *9*, 15561.

[5] a) R. Chollakup, W. Smitthipong, C. D. Eisenbach, M. V. Tirrell, *Macromolecules* **2010**, *43*,5, 2518-2528; b) J. Qin, D. Priftis, R. Farina, S. L. Perry, L. Leon, J. Whitmer, K. Hoffmann, M. V. Tirrell, J. J. de Pablo, *ACS Macro Lett.* **2014**, *3*,6, 565-568; c) E. Spruijt, F. A. M. Leermakers, R. Fokkink, R. Schweins, A. A. van Well, M. A. Cohen Stuart, J. van der Gucht, *Macromolecules* **2013**,*46*,4596-4605; d) F. G. Hamad, Q. Chen, R. H. Colby, *Macromolecules* **2018**, *51*, 15, 5547-5555; e) Q. Wang, J. B. Schlenoff, *Macromolecules* **2014**, *47*, 9, 3108-3116; f) E. Spruijt, A. H. Westphal, J. W. Borst, M. A. Cohen Stuart, J. van der Gucht, *Macromolecules* **2010**, *43*, 6476-6484; g) H. H. Hariri, J. B. Schlenoff, *Macromolecules* **2010**, *43*, 20, 8656-8663; h) I. Varga, R. A. Campbell, *Langmuir* **2017**, *33*, 23, 5915-5924; i) S. De, C. Cramer, M. Schönhoff, *Macromolecules* **2011**, *44*, 22, 8936-8943; j) K. C. Stevens, A. E. Marras, T. R. Campagna, J. M. Ting, M. V. Tirrell, *Macromolecules* **2023**, *56*, 5557-5566.

[6] a) M. Muthukumar, *Macromolecules* **2017**, *50*, 24, 9528-9560; b) H. G. Bungenberg de Jong, H. R. Kruyt, *Proc. K. Ned. Akad. Wet.* **1929** *32*, 849-855; c) S. Srivastava, M. V. Tirrell, Polyelectrolyte Complexation. *Adv. Chem. Phys.* **2016**, *161*, 499-543; d) V. A. Kabanov, *Russ. Chem. Rev.* **2005**, *74*, 3– 20; e) J. van der Gucht, E. Spruijt, M. Lemmers, M. A. Cohen Stuart, *J. Colloid Interface Sci.* **2011**, 361, 407– 422; f) J. Fu, J. B. Schlenoff, *J. Am. Chem. Soc.* **2016**, 138, 980– 990; g) Z. Ou, M. Muthukumar, *J. Chem. Phys.* **2006**, *124*, 154902.

[7] a) S. Chen, Z. Wang, *Proc. Natl. Acad. Sci. U.S.A.* **2022**, *36*, 119; b) S. Adhikari, M. A. Leaf, M. Muthukumar, *J. Chem. Phys.* **2018**, *149*, 163308; c) T. K. Lytle, L. Chang, N. Markiewicz, S. L. Perry, C. E. Sing, *ACS Cent. Sci.* **2019**, *5(4)*,709-718.

[8] a) K. Nishida, K. Kaji, T. Kanaya, *Macromolecules* **1995**, *28*, 2472– 2475; b) M. Muthukumar, *Macromolecules* **2002**, *35*, 9142– 9145; c) C.-L. Lee, M. Muthukumar, *J. Chem. Phys.* **2009**, *130*, 024904; d) K. Shen, Z. G. Wang, *J. Chem. Phys.* **2017**, *146*, 084901.

[9] a) J. Choi, M. F. Rubner, *Macromolecules* **2005**, *38*, 1, 116-124; b) V. S. Meka, M. K. G. Sing, M. R. Pichika, S. R. Nali, V. R. M. Kolapalli, P. Kesharwani, *Drug Discovery Today* **2017**, *22*,11, 1697-1706.

[10] V.S. Rathee, H. Sidky, B. J. Sikora, J. K. Whitmer, *J. Am. Chem. Soc.* **2018**, *140*, 45, 15319-15328.

[11] a) R. Verduzco, X. Li, S. L. Pesek, G. E. Stein, *Chem. Soc. Rev.* **2015**, *44*, 2405-2420; b) J. M. Chan, A. C. Kordon, R. Zhang, M. Wang, *Proc. Natl. Acad. Sci. U.S.A.* **2021**, *118*, 40.

[12] a) S. Dutta, M. A. Wade, D. J. Walsh, D. Guironnet, S. A. Rogers, C. E. Sing, *Soft Matter* **2019**, *15*, 2928-2941; b) S. Rathgeber, T. Pakula, A. Wilk, K. Matyjaszewski, K. L. Beers, *J. Chem. Phys.* **2005**, *122*,124904.

[13] R. Fenyves, M. Schmutz, I. J. Horner, F. V. Bright, J. Rzayev, *J. Am. Chem. Soc*. **2014**, *136*, 21, 7762-7770.

[14] a) M. Iqbal, Y. Tao, S. Xie, Y. Zhu, D. Chen, X. Wang, L. Huang, D. Peng, A. Sattar, M. A. B. Shabbir, H. I. Hussain, S. Ahmed, Z. Yuan, *Biological Procedures Online* **2016**, *18*, 18; b) Z. S. Clauss, C. L. Wardzala, A. E. Schlirf, N. S. Wright, S. S. Saini, B. Onoa, C. Bustamante, J. R. Kramer, *Nature Comm* **2021**,*12*, 6472-6483; c) V. P. Beyer, A. Monaco, R. Napier, G. Yilmaz, C. R. Becer, *Biomacromolecules* **2020**, *21*, 6, 2298-2308; d) X. Banquy, J. Burdyńska, D. W. Lee, K. Matyjaszewski, J. Israelachvili, *J. Am. Chem. Soc*. **2014**, *136*, 17, 6199-6202; e) X. Li, H. ShamsiJazeyi, S. L. Pesek, A. Agrawal, B. Hammouda, R. Verduzco, *Soft Matter* **2014**, *10*, 2008-2015; f) S. Ma, X. Zhang, F. Zhou, *NPG Aisa Materials* **2019**, *11*, 24; g) J. Faivre, B. R. Shrestha, G. Xie, M. Olszewski, V. Adibnia, F. Moldovan, A. Montembault, G. Sudre, T. Delair, L. David, K. Matyjaszewski, X. Banquy, *Chem. Mater*. **2018**, *30*, 12, 4140-4149; h) C. Hörtz, A. Birke, L. Kaps, S. Decker, E. Wächtersbach, K. Fischer, D. Schuppan, M. Barz, M. Schmidt, *Macromolecules* **2015**, *48*, 7, 2074-2086; i) R.J. Dalal, R. Kumar, M. Ohnsorg, M. Brown, T.M. Reineke, *ACS Macro Lett*. **2021**, *10*, 7, 886-893; j) X. Li, B. Wang, Q. Liu, R. Zhao, D.-P. Song, Y. Li, *Langmuir* **2021**, 37, 22, 6744-6753; k) R. J. Dalal, M. L. Ohnsorg, S. Panda, T. M. Reineke, *Biomacromolecules* **2022**, 23, 12, 5179-5192; l) Y. Xia, V. Adibnia, R. Huang, F. Murschel, J. Faivre, G. Xie, M. Olszewski, G. de Crescenzo, W. Qi, Z. He, R. Su, K. Matyjaszewski, X. Banquy, *Angew. Chemie.* **2018**, *131*, 5, 1322-1328; m) K. C. Stevens, M. V. Tirrell, *J. Polym Sci*. **2023**, 1-10.

[15] H. G. Seong, Z. Fink, Z. Chen, T. Emrick, T. P. Russell, *ACS Nano* **2023**, *17*, 15, 14731-14741.

[16] a) A. Yethiraj, *J. Chem. Phys.* **2006**, *125*, 204901; b) H. Zhang, Y. Feng, *J. Appl. Polym. Sci.* **2021**, *138*, 34,50850.

[17] a) M. Wintermantel, M. Schmidt, Y. Tsukahara, K. Kajiwara, S. Kohijiya, *Macromol. Rapid Commun.* **1994**, *15*, 279-284; b) M. Wintermantel, M. Gerle, K. Fischer, M. Schmidt, I. Wataoka, H. Urakawa, K. Kajiwara, Y. Tsukahara, *Macromolecules* **1996**, *29*, 978-983.

[18] a) T. Swift, L. Swanson, M. Geoghegan, S. Rimmer, *Soft Matter* **2016**, *12*, 2542-2549; D. G. Mintis, V. G. Mavrantzas, *J. Phys. Chem. B.* **2019**, *123*, 19, 4204-4219.

[19] A. M. Bapolisi, P. Kielb, M. Bekir, A. C. Lehnen, C. Radon, S. Laroque, P. Wendler, H. M. Muller-Werkmeister, M. Hartlieb, *Macromol. Rapid Commun.* **2022**, *43*, 220028.

[20] S. E. Burke, C. J. Barrett, *Pure Appl. Chem.* **2004**, *76*, 1387-1398.

[21] L. Li, S. Srivastava, S. Meng, J. M. Ting, M. V. Tirrell, *Macromolecules* **2020**, *53*, 7835-7844.

[22] T. K. Lytle, C. E. Sing, *Soft Matter* **2017**, *13(39)*, 7001-7012.

[23] M. G. Wessels, A. Jayaraman, *Soft Matter* **2019**, *15*, 3987-3998.

[24] a) P. M. Biesheuvel, M. A. Cohen Stuart, *Langmuir* **2004**, *20*, 7, 2785-2791; b) H. Dautzenberg, J. Kriz, *Langmuir* **2003**, *19*, 13, 5204-5211.

[25] D. W. Schaefer, R. S. Justice, *Macromolecules* **2007**, *40*, 24, 8501-8517.

[26] a) A. S. Utada, A. Fernandez-Nieves, H. A. Stone, D. A. Weitz, *Phys. Rev. Lett.* **2007**, *99*, 094502; b) H. C. Shum, J. Varnell, D. A. Weitz, *Biomicrofluidics* **2012**, *6*, 012808-012808-9.

[27] S. Zhu, J. Forth, G. Xie, Y. Chao, J. Tian, T. P. Russell, H. C. Shum, *ACS Nano* **2020**, *14 (9)*, 11215-11224.

[28] a) K. D. Kelly, J. B. Schlenoff, *ACS Appl. Mater. Interfaces.* **2015**, *7*, 25, 13980-13986; b) D. Scheepers, A. Casimiro, Z. Borneman, K. Nijmeijer, *ACS Appl. Polym. Mater.* **2023**, *5*, 3, 2032-2042; c) Q. Ma, H. Yuan, Y. Song, Y. Chao, S. Y. Mak, H. C. Shum, *Soft Matter* **2018**, *14*, 1552-1558; d) L. Zhang, L. H. Cai, P.S. Lienemann, T. Rossow, I. Polenz, Q. Vallmajo-Matrin, M. Ehrbar, H. Na, D. J. Mooney, D. A. Weitz, *Angew. Chem. Int. Ed. Engl.* **2016**, *55*, 13470-13474.

[29] G. A. Parada, H. Yuk, X. Liu, A. J. Hsieh, X. Zhao, *Adv. Healthcare Mater*. **2017**, *6*, 1700520.

[30] C. T. Culbertson, S. C. Jacobson, J. M. Ramsey, *Talanta* **2002**, *56*, 2, 365-373.

[31] L. T. Hirschwald, S. Brosch, G. Linz, J. Linkhorst, M. Wessling, *Adv. Mater. Technol.* **2023**, *8*, 2201857.

[32] Y. Chao, H. C. Shum, *Chem. Soc. Rev.* **2020**, *49*, 114-142.

[33] A. A. Antipov, G. B. Sukhorukov, E. Donath, H. Möhwald, *J. Phys. Chem. B.* **2001**, *105*, 12, 2281-2284.

[34] a) P. K. Walhout, Z. He, B. Dutagaci, G. Nawroki, M. Feig, *J. Phys. Chem. B.* **2022**, *126*, 48, 10256-10272; b) G. S. Offeddu, L. Mohee, *Journal of Materials Science: Materials in Medicine* **2020**, *31*,46.

[35] B. M. DeVetter, S. T. Sivapalan, D. D. Patel, M. V. Schulmerich, C. J. Murphy, R. Bhargava, *Langmuir* **2014**, *30*, 29, 8931-8937.

[36] a) S. Eikenberry, *Theor Biol Med Model* **2009**, *6*, 16; b) M. Fernandez-Chas, M. J. Curtis, S. A. Niederer, *Br J Pharmacol.* **2018**, *175(5)*, 763-781; c) M. Arzt, B. Gao, M. Mozneb, S. Pohlman, R. B. Cejas, Q. Liu, F. Huang, C. Yu, Y. Zhang, X. Fan, A. Jenkins, A. F. Ciuliano, P. W. Burridge, X. Cui, A. Sharma, *Stem Cell Report* **2023**, *18*, 1913-1924.

[37] a) D. Ferreira, R. Bachelard, W. Guerin, R. Kaiser, M. Fouché, *American Jol. Of Phys.* **2020**, 88,10,831-837; b) J. Zmpitas, J. Gross, *Ind. Eng. Chem. Res.* **2021**, 60, 11, 4453-4459.

[38] a) P. J. Wyatt, Light Scattering and the absolute characterization of macromolecules, *Anal. Chim. Acta* **1993**, *272*, 1-40; b) T. Takagi, *J. Chromatogr* **1990**, *506*, 409-416.

[39] a) K. S. Schmitz, An introduction to Dynamic Light Scattering by Macromolecules, Academic Press: San Diego,1990; b) B. J. Berne, R. Pecora, Dynamic Light Scattering Dover: New York, 1976.

[40] H. Zhang, Y. Feng, *J. Appl. Polym. Sci.* **2021**, *138*, 34, 50850.

[41] a) O. F. Solomon, I. Z. Ciutã, *J. Appl. Polym. Sci.* **1962,** *6*, 24,683-686; b) E. O. Kraemer, *Ind. Eng. Chem.* **1938**, *30*, 1200-1203; c) M. I. Huggins, *J. Am. Chem. Soc.* **1942**, *64*, 11, 2716-2718; d) M. W. Wallach, *J. Polym. Sci., A-2* **1967**, *5*, 653-662; e) T. Bibire, O. Yilmaz, C. M. Ghiciuc, N. Bibire, *Coatings* **2022**, *12*, 2, 211; f) R. Rebelo, M. Fernandes, R. Fangueiro, *Procedia Engineering* **2017**, 200, 236-243; g) K. Terao, T. Hokajo, Y. Nakamura, T. Norisuye, *Macromolecules* **1999**, 32, 3690-3694; h) S. E. Harding, *Prog. Biophys. Molec. Biol.* **1997**, 68, 207-262.

[42] a) J. Zhao, C. Qi, G. Li, M. A. Schmidt, *Phys. Chem. Chem. Phys.* **2020**, *22*, 21784; b) S. Jana, S. Ghosh, S. Nath, S. Pande, S. Praharaj, S. Panigrahi, S. Basu, T. Endo, T. Pal, *Appl. Catal., A* **2006**, *313*, 41– 48; c) Z. Chen, M. Hu, X. Li, D. M. Smith, H. G. Seong, T. Emrick, J. Rzayev, T. P. Russell, *Angew. Chem. Int. Ed*. **2022**, *61*, e202201392.

Entry for the Table of Contents

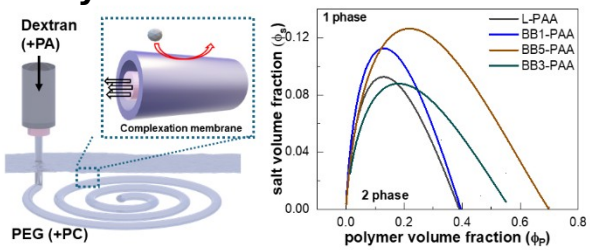

A new polyelectrolyte complex, comprising anionic bottlebrush polymer and cationic linear polymer, exhibits a broader phase separation diagram and higher salt resistance capacity and vary spherical-like to core-shell-like conformation. Utilizing this system creates a tubular-like flow structure at the interface of two aqueous liquids, enhancing the structural stability, offering a more efficient and easy method for particle transport.